Observation of squeeze-twist coupling in a chiral three-dimensional isotropic lattice

Jianheng Li†, Chan Soo Ha+, Roderic S. Lakes*

Department of Engineering Physics, University of Wisconsin, Madison, WI 53706-1687, USA
Keywords (isotropy, chirality, negative Poisson's ratio, auxetic, Cosserat)
∗ Corresponding author. email lakes@engr.wisc.edu Phone: +00 608 265 8697
+ hachansoo0413@gmail.com
† University of California, Davis. email jheli@ucdavis.edu

J. Li, C. S. Ha, R. S. Lakes, Observation of squeeze twist coupling in a chiral three-dimensional isotropic lattice, Physica Status Solidi B Volume 257, Issue 10, 1900140, October (2020).

Abstract

A chiral 3D lattice was designed, made by 3D printing, and studied experimentally. The lattice exhibited squeeze-twist coupling and a Poisson's ratio near zero. Squeeze-twist coupling does not occur in classical elasticity which makes no provision for chirality. By contrast, chiral effects are allowed in Cosserat elasticity. An experimental squeeze-twist coupling strain ratio on the order of unity and a Poisson's ratio near zero are in reasonable agreement with prior finite element analysis of a lattice with similar structure, for which negative Poisson's ratio is anticipated for a sufficient number of cells.

1 Introduction

Chirality refers to the handedness of a material or a structure. Chiral materials occur in left- and right-handed forms. Effects of chirality have long been known in optics. In optically active materials there is a rotation of the plane of polarization of linearly polarized light as it passes through the material [1]. Optically active materials must be chiral [2] [3]. Directional anisotropy and chirality are independent concepts. A material can be chiral and directionally isotropic, as in liquids or gases that contain chiral molecules. Sugar molecules are chiral as are solutions with dissolved sugar; quartz crystals are chiral on the interatomic scale. Many organic compounds including amino acids and some biologically active compounds used as drugs are chiral [4]. Physical properties such as piezoelectricity and pyroelectricity require chirality for them to occur [2].

Piezoelectric and pyroelectric properties are described by tensors of odd rank so a non-chiral material that is invariant to coordinate inversions cannot exhibit these properties. Chirality has no effect in classical elasticity because the elasticity tensor is of even (fourth) rank. Inversion of coordinates has no effect on the elastic modulus tensor. Strictly, classical elasticity requires the structural elements to be vanishingly small. Even so, most analyses of cellular solids such as honeycombs and foams (e.g. [5]) and of truss lattices [6] assume classical elasticity. Classical elasticity has no length scale. Nevertheless one may envisage chiral elastic solids. A 2D chiral lattice with Poisson's ratio -1 independent of strain [7] was developed, analyzed and studied experimentally.

Chiral 2D lattices have been studied [8] [9] for possible application in sandwich panels for shape-changing airplane wings. In the context of possible structural applications, studies have been done of buckling [10] [11] deformation of chiral 2D lattices. Chiral 2D lattices with sensors and actuators [12] have been considered as smart structures. These lattices have been studied in the context of reducing vibration [13].

As for elastic 3D materials, effects of chirality on elastic response are predicted [14] provided one allows more freedom than in classical solids. A variety of generalized continuum theories are known that incorporate such additional freedom. Cosserat [15] [16] (or micropolar [17]) elasticity, in contrast to classical elasticity, allows characteristic length scales within a continuum description. Such an approach is warrantable when the size scale of specimens does not exceed the microstructure size by too large a factor. In a Cosserat solid, stress concentrations around holes are lower than in a classical solid. Also, size effects occur in which slender bars in torsion or bending are stiffer than expected classically. Coupling between axial stretch or compression and twisting deformation is predicted in a chiral solid [14]. Indeed stretch-twist coupling effects were observed in slender samples of bone [21] and in tendon fascicles [22].

The constitutive equations [17] for linear isotropic (non-chiral) Cosserat elasticity are

$$\sigma_{ij} = 2G\epsilon_{ij} + \lambda\epsilon_{kk}\delta_{ij} + \kappa e_{ijk}(r_k - \phi_k) \tag{1}$$

$$m_{ij} = \alpha\phi_{k,k}\delta_{ij} + \beta\phi_{i,j} + \gamma\phi_{j,i}. \tag{2}$$

The stress σ_{ij} (force per unit area) is in general asymmetric. The resulting moment is balanced by a couple stress m_{ij} (a torque per unit area). Here, ϕ_m is the rotation of points, called micro-rotation, e_{ijk} is the permutation symbol, and $r_k = \frac{1}{2}e_{klm}u_{m,l}$ is "macro"-rotation based on the antisymmetric part of the gradient of displacement u_i. Also δ_{ij} is the Kronecker delta and ϵ_{ij} is the strain tensor. The usual Einstein summation convention for repeated indices is used.

The quantities λ, G are classical elastic constants. Elastic constants α, β, γ govern the characteristic length scales at which nonclassical effects are to be observed. κ is an elastic constant that quantifies the degree of coupling between micro- and macro-rotations. There are six independent Cosserat elastic constants. They may be expressed for physical insight as technical elastic constants, Young's modulus E, shear modulus G, Poisson's ratio ν, characteristic length in torsion ℓ_t, characteristic length in bending ℓ_b, coupling number N, polar ratio Ψ. They are:

$$E = \frac{2G(3\lambda + 2G)}{2\lambda + 2G} \tag{3}$$

$$\nu = \frac{\lambda}{2\lambda + 2G} \tag{4}$$

$$\ell_t = \sqrt{\frac{\beta + \gamma}{2G}} \tag{5}$$

$$\ell_b = \sqrt{\frac{\gamma}{4G}} \tag{6}$$

$$N = \sqrt{\frac{\kappa}{2G + \kappa}} \tag{7}$$

$$\Psi = \frac{\beta + \gamma}{\alpha + \beta + \gamma}. \tag{8}$$

The case $N = 1$ corresponding to $\kappa \to \infty$ is equivalent to a strain gradient theory, at times called couple stress elasticity [18]. Nonlocal elasticity [19] entails stress that depends not only on

the strain at a point but also on the strain in a region surrounding that point. Nonlocal elasticity can be specialized to a differential form that entails an approximation to the nonlocal integral [19]. This approximation allows sensitivity to gradients of the stress or strain so it is equivalent to a gradient theory. Starting from a composite structure, one can determine nonlocal characteristics [20], but no known methods are available to extract full nonlocal properties from experimental data. Because such methods are available for Cosserat elasticity, we use that approach to interpret experiments.

The constitutive equations for a chiral Cosserat solid which is isotropic with respect to direction but is not invariant with respect to inversions are [14]:

$$\sigma_{kl} = \lambda\epsilon_{rr}\delta_{kl} + 2G\epsilon_{kl} + \kappa e_{klm}(r_m - \phi_m) + C_1\phi_{r,r}\delta_{kl} + C_2\phi_{k,l} + C_3\phi_{l,k} \tag{9}$$

$$m_{kl} = \alpha\phi_{r,r}\delta_{kl} + \beta\phi_{k,l} + \gamma\phi_{l,k} + C_1\epsilon_{rr}\delta_{kl} + (C_2 + C_3)\epsilon_{kl} + (C_3 - C_2)e_{klm}(r_m - \phi_m). \tag{10}$$

Elastic constants C_1, C_2 and C_3 are associated with the effect of chirality (i.e., noncentrosymmetry). An exact solution for tension / compression of a round chiral isotropic Cosserat rod [14] may be used as a guide in seeking new effects including stretch-twist coupling, size effects in tension or compression stiffness, and size effects in Poisson's ratio. While it is possible to obtain all six elastic constants of an isotropic Cosserat solid via experiment [23] [24], available analysis does not currently suffice to determine all nine constants of a 3D chiral solid from experiment.

Poisson's ratio in classical elasticity is not influenced by chirality because classical elasticity itself is not sensitive to chirality. In an isotropic three dimensional Cosserat solid [17], the allowable range of Poisson's ratio is the same as in a classical 3D solid, from -1 to 1/2. Both negative Poisson's ratio and chirality depend on the structure of a solid, but different aspects of structure. Negative Poisson's ratio (-0.7 to -0.8) of (3D) foams [25] [26] (called "anti-rubber" [27]) and of (2D) honeycombs [28] is based on a folded in or re-entrant structure that allow empty space to easily open up in the structure. Two-dimensional structures with rotating hexamers [29] [30] or trimers [31] or hinged rotating squares [32] give rise to a negative Poisson's ratio. Rotation of structural elements in microporous polyethylene [33] gives rise to negative Poisson's ratio called "auxetic". Lattices with a negative Poisson's ratio were designed in 3D [34] and fabricated; the Poisson's ratio -0.8 was comparable to that of the metal [26] re-entrant foams. Materials with Poisson's ratio approaching the lower limit are called "dilational" [35].

These, and many other examples of negative Poisson's ratio materials that have since been demonstrated are not chiral. As for 2D chiral lattices [7], these have been analyzed [36] [37] in the context of Cosserat elasticity to determine some of the nonclassical elastic constants. 3D chiral lattices [38] with cubic structure and tunable Poisson's ratio were designed and were shown via finite element analysis to be Cosserat elastic. They contain cubical nodules with ribs in a chiral arrangement. Chirality in 3D gives rise to stretch twist coupling [14] that is absent in 2D materials and structures. By tuning the aspect ratio of nodule center spacing to nodule width, the lattices were designed to be elastically isotropic [39]. Elastic isotropy allows simpler interpretation of both analysis and experiment than if the solid were highly anisotropic. The aspect ratio, defined as the ratio of nodule center spacing to cubical nodule width, was 1.64.

In the present research, an elastically isotropic 3D chiral lattice [39] was redesigned for physical realization and was embodied via 3D printing. The lattice was studied experimentally via a digital image correlation technique. Study of the deformation field revealed Poisson's ratio and squeeze-twist coupling, which can only occur in a chiral material. The effect was interpreted via Cosserat theory. Measured Poisson's ratio and squeeze-twist coupling from experiment were compared with values from numerical methods [39].

2 Methods

Conceptual models of the chiral lattice were envisaged, then constructed in Solidworks, (Figure 1). The shape was converted to STL format and 3D printed via the Fused Deposition Modeling (FDM) method. This method uses a polymer raw material filament that is fed through a heated nozzle. The nozzle extrudes a thin melted filament which is laid down in layers and which solidifies under ambient conditions. The printer was a Dimension Elite 3D printer. The claimed minimum feature size was 0.51 mm. The resolution was about 0.2 mm. The parent material was ABS plus P430 (Young's modulus E of 2.2 GPa and yield stress of 31 MPa). It was found that the ribs had to be sufficiently thick compared with the printer resolution and minimum feature size for the physical lattice to have structural integrity. This requirement is in contrast to finite element analysis of a chiral lattice [39] in which rib thickness does not matter. The final lattice had five cells in each direction. Each cubical nodule had a side length of one centimeter. The rib diameter was 2 mm. The spacing of the nodules was chosen to achieve elastic isotropy following finite element analysis [39]. The analysis assumed rigid cubical nodules connected by slender flexible ribs. The rib length was varied to achieve elastic isotropy. Size effects and squeeze-twist coupling were then explored numerically. The requisite aspect ratio is 1.64 so the distance between nodule centers was 1.64 cm. The lattice is shown in Figure 2.

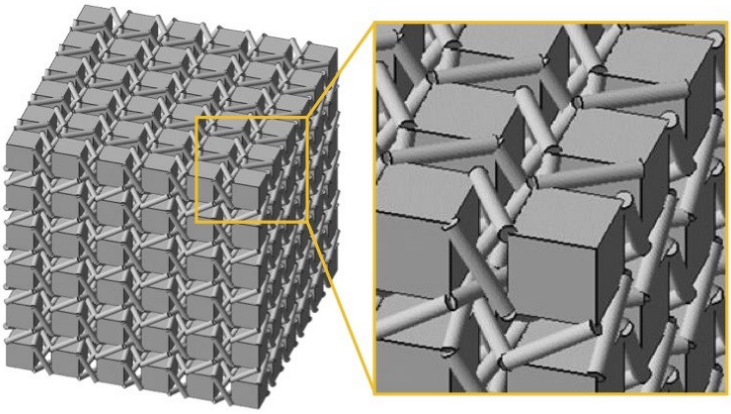

Figure 1: Design of chiral 3D lattice.

Because the parent material comprising the lattice is ABS plastic for which Young's modulus is 2.2 GPa, the lattice is sufficiently stiff that, in contrast to elastomer foams, the lattice does not deform visibly when pressed by hand.

The 3D printed lattice differed from the finite element model [39] in that it was expedient for the physical ribs to have their center line aligned with the cube corners, as shown. So the ribs extended beyond the surface of the cubical nodules. Also, the physical ribs could not be made arbitrarily slender. To allow the compression to be applied to the nodules and not to the ribs, an adapter plate was designed and made for the top and bottom surfaces of the specimen, 3D printed using the same polymer as that used to make the lattice. The plate, shown in Figure 3, was provided with square protrusions to match the spacing of the cubical nodules in the lattice.

Load was applied using dead weights manually applied slowly. In contrast to a test frame which would restrict rotational motion from squeeze-twist coupling, dead weights offer zero resistance to rotation. The adapter plate was free to rotate so it could not constrain rotation. Some constraint of the distribution of end deformation is possible, but the adapter plate was made of the same

polymer as the lattice. No glue was used. Such constraint was therefore not considered a matter of concern. The applied loads for this experiment were 10 pounds (44 N) and 30 pounds (134 N).

Digital Image Correlation (DIC) was used to measure the deformation. DIC is a technique which incorporates digital image processing in order to analyze small deformations in objects. The instrument in the 2D embodiment used contains a black and white camera of resolution 5 megapixels used to obtain digital images of the test object in undeformed and deformed conditions. Pictures are then analyzed using software (VIC2D) to determine the deformation field from the images. The algorithm of DIC traces specific patterned dots on the object before and after the load is applied. Therefore a pattern of speckles on one surface of the object is necessary to ensure that DIC can detect the small deformation. The pattern can be produced either by covering the surface with black sticky powders or by making dots with a pen. Such a pattern is shown on one surface of the lattice shown in Figure 2. In the present study, a single camera was used to reveal the vertical component and one horizontal component of deformation.

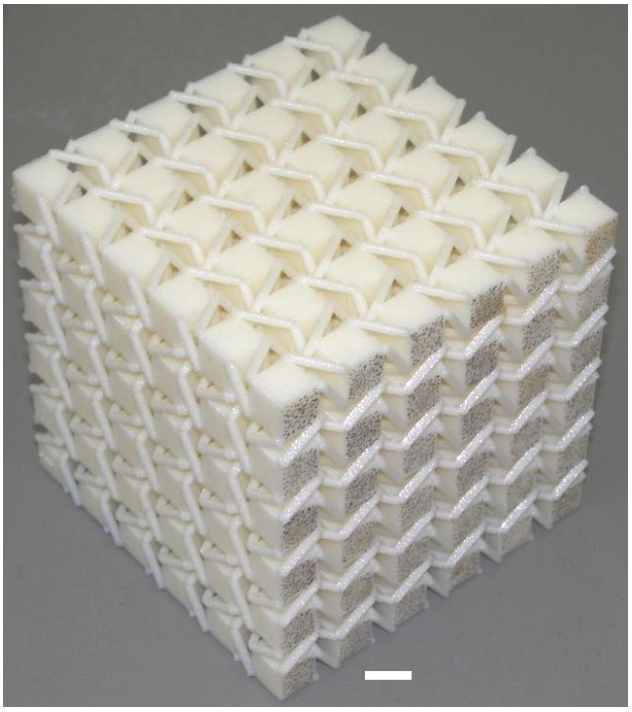

Figure 2: Chiral 3D lattice. Scale bar: 10 mm.

Because the parent material comprising the lattice is ABS plastic for which Young's modulus is 2.2 GPa, the lattice is sufficiently stiff that, in contrast to elastomer foams, the lattice does not deform visibly when pressed by hand.

The 3D printed lattice differed from the finite element model [39] in that it was expedient for the physical ribs to have their center line aligned with the cube corners, as shown. So the ribs extended beyond the surface of the cubical nodules. Also, the physical ribs could not be made arbitrarily slender. To allow the compression to be applied to the nodules and not to the ribs, an adapter plate was designed and made for the top and bottom surfaces of the specimen, 3D printed using the same polymer as that used to make the lattice. The plate, shown in Figure 3, was provided with square protrusions to match the spacing of the cubical nodules in the lattice.

Load was applied using dead weights manually applied slowly. In contrast to a test frame which

would restrict rotational motion from squeeze-twist coupling, dead weights offer zero resistance to rotation. The adapter plate was free to rotate so it could not constrain rotation. Some constraint of the distribution of end deformation is possible, but the adapter plate was made of the same polymer as the lattice. No glue was used. Such constraint was therefore not considered a matter of concern. The applied loads for this experiment were 10 pounds (44 N) and 30 pounds (134 N).

Digital Image Correlation (DIC) was used to measure the deformation. DIC is a technique which incorporates digital image processing in order to analyze small deformations in objects. The instrument in the 2D embodiment used contains a black and white camera of resolution 5 megapixels used to obtain digital images of the test object in undeformed and deformed conditions. Pictures are then analyzed using software (VIC2D) to determine the deformation field from the images. The algorithm of DIC traces specific patterned dots on the object before and after the load is applied. Therefore a pattern of speckles on one surface of the object is necessary to ensure that DIC can detect the small deformation. The pattern can be produced either by covering the surface with black sticky powders or by making dots with a pen. Such a pattern is shown on one surface of the lattice shown in Figure 2. In the present study, a single camera was used to reveal the vertical component and one horizontal component of deformation.

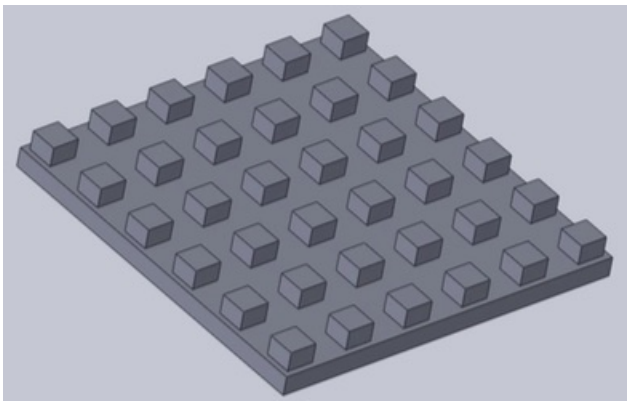

Figure 3: Adapter plate to apply compression to the cubical nodules in the lattice.

Young's modulus was calculated by subtracting the average displacement at the bottom from the average displacement at the top to eliminate the effect of the support compliance. This was necessary because it was observed that the bottom adapter plate underwent some vertical motion when load was applied to the top. The supporting table was therefore not infinitely rigid in comparison with the specimen. Specimen end vertical displacement was calculated from an average of the displacements of the individual cubical nodules along the top and the bottom respectively. Poisson's ratio was determined from the averages of the ratio of average horizontal strain to vertical strain. The averages were computed manually from the nodule displacements rather than by use of a further algorithm. The inference of modulus was done using the elementary analysis for compression, $E = \sigma/\epsilon = (F/A)/(\Delta L/L)$ with F as force, A as cross section area, L as length, and the displacement ΔL as change in length considered as an average. Strain was not used as an intermediate; force and displacement were used directly.

3 Results and Discussion

Representative images of the digital image correlation output are shown in Figure 4 and Figure 5. The numbers in Figure 4 represent the vertical component of the displacement of each nodule center in millimeters. The numbers in Figure 5 represent the horizontal component. Each such image provided 36 values of displacement. The process was repeated for two load levels. Determination of Poisson's ratio (Table 1 and Figure 6) and of twist due to compression (Table 1) entails use of both vertical and horizontal displacement values as described above. It was not necessary to explicitly determine strain as an intermediate.

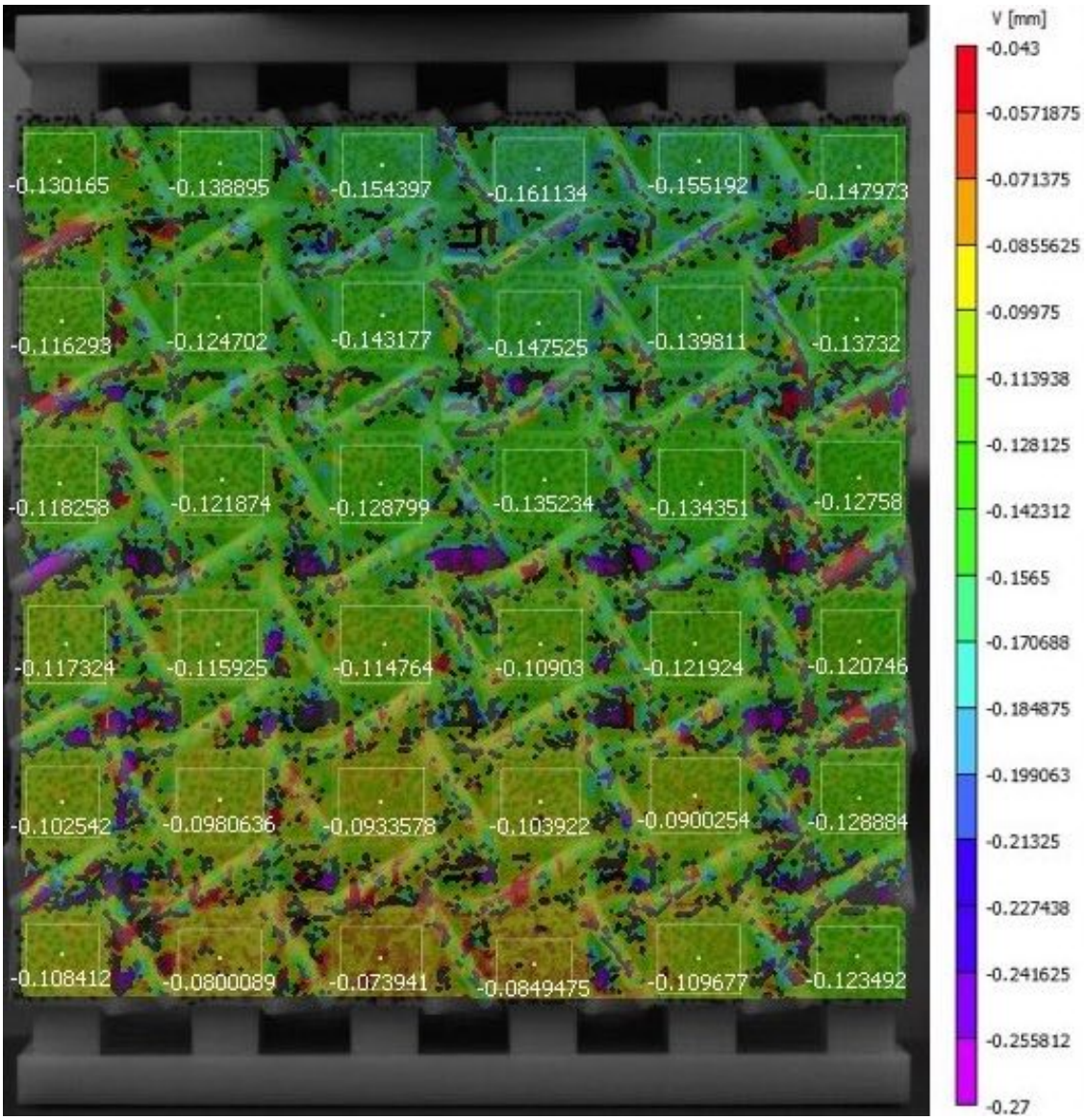

Figure 4: Visual output of digital image correlation: vertical motion. Numbers correspond to the vertical component of displacement in millimeters.

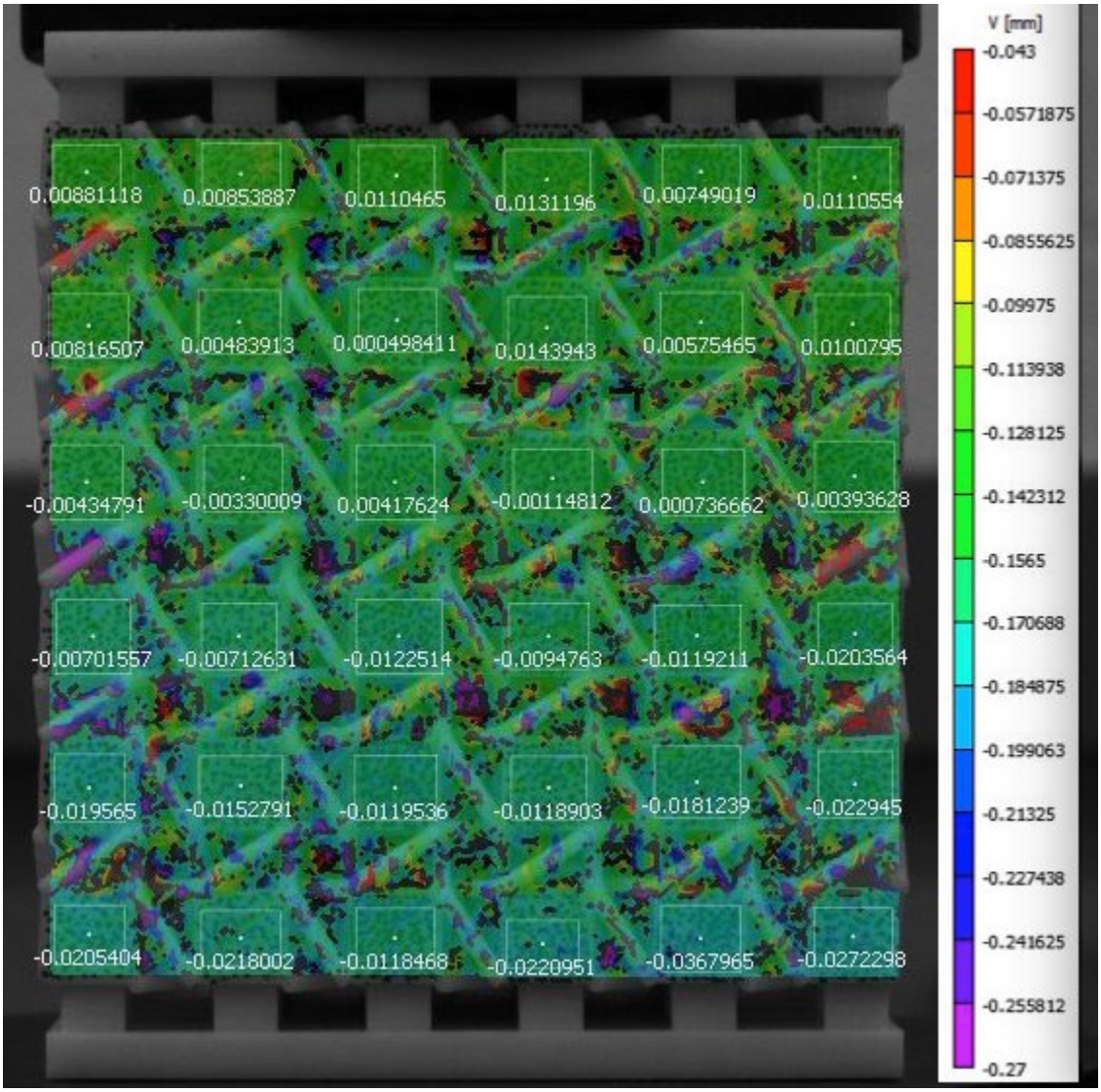

Figure 5: Visual output of digital image correlation: horizontal motion. Numbers correspond to the horizontal component of displacement in millimeters.

Properties determined from the available single specimen are considered to be effective properties in view of the size effects obtained via finite elements [39] and size effects observed experimentally in other materials. Intrinsic moduli and Poisson's ratio would require specimens with an asymptotically large number of cells. The Poisson's ratio ν was observed to be close to zero in reasonable agreement with finite element analysis of the lattice as shown in Table 1. The magnitude of squeeze-twist coupling, expressed as a ratio of peak strains in shear γ to that in compression ϵ of the surface was similar to that predicted by finite element analysis, on the order unity, for a specimen five cells on a side.

The observed Young's modulus E was somewhat smaller than that predicted and the value showed a slight dependence on load level. This is not surprising in view of the fact the 3D printed lattice had a rib geometry that could not be made identical to that in the analysis due to fabrication imperfections. Also, the cubical configuration does not allow the usual assumption of Saint Venant's

Table 1: Lattice properties from experiment at two load levels compared with results from finite element method (FEM) [39]. Effective Young's modulus E, Poisson's ratio ν, and twist-stretch ratio γ/ϵ of strains.

–	E(MPa)	ν	γ/ϵ
FEM	62	0.01	0.99
Experiment 10 lb	56	-0.03	0.96
Experiment 30 lb	57	0.05	1.47

principle in which the details of load application at the ends are ignored. Because end effects can occur in the experiment in contrast to the analysis, the inferred modulus is expected to differ. The deformation field is heterogeneous. Some of the heterogeneity arises from the lattice structure. Heterogeneity also arises from the method of load application. The load in the finite element analysis [39] was applied with exact same magnitude of force on each cubical nodule because it was possible to assume a perfect boundary condition. However, in the experiment, the application of dead weight, even with the heat-sink shaped end plates, cannot be exactly evenly distributed. That difference can be responsible for part of the load dependence and difference with respect to the analysis. Also, the analysis assumed the cubical nodules to be rigid in contrast to the experiment in which the nodules are made of the same deformable material as the ribs. Not much difference is expected from that assumption of rigidity because a solid cube will be much less deformable than a thin rib of the same material. A greater effect on the modulus of the experimental lattice is expected from the fact the ribs were attached to the cube corners by their edges. The apparent load dependence of inferred properties is attributed primarily to contact deformation of the adapter plates. The inferred compressive strain is less than 0.0004, well within the linear range of behavior for the polymer used. The difference in inferred properties with applied load is therefore interpreted as an error bar.

The observed Poisson's ratio is compared with results of finite element analysis [39] of different specimen sizes in Figure 6. Poisson's ratio tends to a negative value for a specimen containing a sufficient number of cells. It was not practical to approach the asymptotic value of negative Poisson's ratio in experiments because that would require more cells than could readily be produced with available printers. A corresponding limitation in the finite element analysis was encountered: computing resources limited the number of cells. Such limitations are likely to become less stringent in the future.

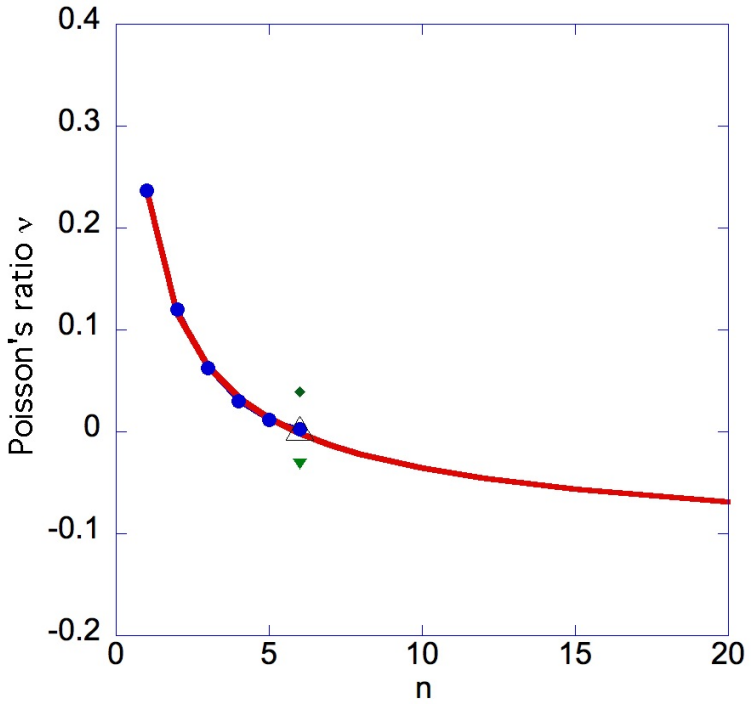

Figure 6: Poisson's ratio vs. specimen width in number n of cubical nodules along each edge. Comparison of results of analysis [39] (circles) and experiment (inverted triangle, 10 pound load; diamond, 30 pound load; large open triangle, average.) The solid line represents a curve fit to the analytical points and an extrapolation of the analysis to a larger number of cells.

The Poisson's ratio depends on specimen size for chiral materials as anticipated from the 3D continuum analysis [14]. The squeeze-twist coupling also depends on specimen size via analysis.

Chiral 2D and 3D lattices allow a negative Poisson's ratio via rotation of the nodules. In 2D, an unrolling action gives rise to a Poisson's ratio of -1 essentially independent of strain [7]. In 3D, Poisson's ratio of the lattice under study can become negative for a sufficient number of cells in the cross section. The specimen studied in the experiments had a Poisson's ratio near zero, in agreement with the finite element analysis [39]. The allowable range of Poisson's ratio is the same for classical and Cosserat elasticity and is not directly influenced by chirality. The negative Poisson's ratio in the lattices is a result of the structure of the cells.

The size scale of the experiment was constrained by the size scale of the lattice which in turn was limited by the resolution of the 3D printer. Chirality can occur on a variety of size scales. Chirality, as is known, can occur on the scale of interatomic bonds as is the case in quartz and in sugar. Chiral cholesteric elastomers [40] were predicted to have a characteristic length on the order of 10 nm; they were predicted to twist in response to stretching. Selenium and tellurium are chiral elements that are piezoelectric semiconductors [41]. This chirality occurs on the scale of the atomic lattice. Stretch-twist coupling due to elastic chirality on such a fine scale may be detectable; very small twist is detectable as in the Cavendish balance. Size scales associated with elastic chirality are also pertinent to unusual isotropic piezoelectric solids [42] for which polarization is coupled via an isotropic third rank tensor to the antisymmetric part of the stress.

Chiral elastic response may be of interest in the context of sensors and actuators; also in the understanding of natural materials such as bone, wood, and fibrous proteins.

4 Conclusion

Twisting deformation in response to compressive load is observed in a chiral lattice. Such twist-squeeze coupling cannot be understood within classical elasticity but is predicted to occur in a chiral Cosserat solid. Squeeze-twist ratio and Poisson's ratio are in reasonable agreement with finite element analysis of a lattice with similar structure.

References

[1] J. C. Bose, On the rotation of plane of polarisation of electric waves by a twisted structure, Proc. Royal Society of London, **63**, 146-152, (1898).

[2] J. F. Nye, *Physical Properties of Crystals*, Oxford, Clarendon, (1976).

[3] D. R. Lovett, *Tensor Properties of Crystals*, Adam Hilger, Bristol and Philadelphia, (1989).

[4] R. Bentley, From Optical Activity in Quartz to Chiral Drugs: Molecular Handedness in Biology and Medicine, Perspect. Biol. Med. **38** (2), 188-229 (1995).

[5] L. J. Gibson, and M. F. Ashby, *Cellular Solids*, 2nd Ed., Cambridge University Press, Cambridge, (1997).

[6] V. Deshpande, N. Fleck and M. F. Ashby, Effective properties of the octet truss lattice material, Journal of the Mechanics and Physics of Solids **49**, 1747-1769, (2001).

[7] D. Prall and R. S. Lakes, Properties of a chiral honeycomb with a Poisson's ratio -1, Int. J. of Mechanical Sciences, **39**, 305-314, (1996).

[8] D. Bornengo, F. Scarpa, C. Remillat, Evaluation of hexagonal chiral structure for morphing airfoil concept, Proceedings of the Institution of Mechanical Engineers, Part G: Journal of Aerospace Engineering **219** 185-192 (2005).

[9] J. Martin, J. Heyder-Bruckner, C. Remillat, F. Scarpa, K. Potter, M. Ruzzene, The hexachiral prismatic wingbox concept, Phys. Stat. Sol. (b) **245** 570-571 (2008).

[10] A. Spadoni, M. Ruzzene and F. Scarpa, Global and local linear buckling behavior of a chiral cellular structure, Phys. Stat. Sol. (b) **242** 695-709 (2005).

[11] W. Miller, C. W. Smith, F. Scarpa, K.E. Evans, Flatwise buckling optimization of hexachiral and tetrachiral honeycombs, Composites Science and Technology, **70**, 1049-1056, (2010).

[12] H. Abramovitch, M. Burgard, L. Edery-Azulay, K.E. Evans, M. Hoffmeister, W. Miller, F. Scarpa, C.W. Smith, K.F. Tee, Smart tetrachiral and hexachiral honeycomb: Sensing and impact detection, Composites Science and Technology **70**, 1072-1079 (2010).

[13] A. Spadoni, M. Ruzzene, S. Gonelli, F. Scarpa, Phononic properties of hexagonal chiral lattices, Wave Motion **46** (7), 435-450 (2009).

[14] R. S. Lakes and R. L. Benedict, Noncentrosymmetry in micropolar elasticity, International Journal of Engineering Science, **29** (10), 1161-1167, (1982).

[15] E. Cosserat, and F. Cosserat, *Theorie des Corps Deformables*, Hermann et Fils, Paris (1909).

[16] R. D. Mindlin, Stress functions for a Cosserat continuum, Int. J. Solids Structures, **1**, 265-271 (1965).

[17] A. C. Eringen, Theory of micropolar elasticity. In *Fracture* Vol. **1**, 621-729 (edited by H. Liebowitz), Academic Press, New York, (1968).

[18] W. T. Koiter, Couple-Stresses in the theory of elasticity, Parts I and II, Proc. Koninklijke Ned. Akad. Wetenshappen **67**, 17-44 (1964).

[19] A. C. Eringen, On differential equations of nonlocal elasticity and solutions of screw dislocations and surface waves, J. Appl. Phys. **54**, 4703-4710 (1983).

[20] W. J. Drugan, Two Exact Micromechanics-Based Nonlocal Constitutive Equations for Random Linear Elastic Composite Materials, Journal of the Mechanics and Physics of Solids **51**, 1745-1772 (2003).

[21] R. S. Lakes, Is bone elastically noncentrosymmetric?, Proc. 34th ACEMB. Houston (1981).

[22] K. Buchanan, R. S. Lakes, R. Vanderby, Chiral behavior in rat tail tendon fascicles, Journal of Biomechanics, **64**, 206-211 (2017).

[23] R. S. Lakes, Experimental microelasticity of two porous solids, Int. J. Solids and Structures, **22** 55-63 (1986).

[24] Z. Rueger and R. S. Lakes, Strong Cosserat elasticity in a transversely isotropic polymer lattice, Physical Review Letters, **120**, 065501 (2018).

[25] R. S. Lakes, Foam structures with a negative Poisson's ratio, Science, **235** 1038-1040 (1987).

[26] J. B. Choi and R. S. Lakes, Nonlinear properties of metallic cellular materials with a negative Poisson's ratio, J. Materials Science, **27**, 5373-5381 (1992).

[27] J. Glieck, Anti-rubber, The New York Times, 14 April (1987).

[28] L. J. Gibson, M. F. Ashby, G. S. Schajer, and C. I. Robertson, The mechanics of two dimensional cellular solids, Proc. Royal Society London, **A382**, 25-42 (1982).

[29] K. W. Wojciechowski, Constant thermodynamic tension Monte Carlo studies of elastic properties of a two-dimensional systems of hard cyclic hexamers, Molecular Physics, **61**, 1247-125 (1987).

[30] K. W. Wojciechowski, Two-dimensional isotropic systems with a negative Poisson ratio, Physics Letters **A137**, 60-64 (1989)

[31] A. A. Pozniak and K. W. Wojciechowski, Poisson's ratio of rectangular anti-chiral structures with size dispersion of circular nodes, Phys. Stat. Sol. (b) **251**, 367-374, (2014).

[32] J. N. Grima and K. E. Evans, Auxetic behavior from rotating squares, J. Mater. Sci. Lett. **19** 1563-1565 (2000).

[33] K. L. Alderson, A. P. Kettle, K.E. Evans, Novel fabrication route for auxetic polyethylene. Part 1. Processing and microstructure, Polymer Engineering and Science, **45**, 4, 568-578, (2005).

[34] T. Buckmann, R Schittny, M Thiel, M Kadic, GW Milton and M Wegener, On three-dimensional dilational elastic metamaterials, New Journal of Physics **16** 033032 (2014).

[35] G. Milton, Composite materials with Poisson's ratios close to -1, J. Mech. Phys. Solids, **40**, 1105-1137, (1992).

[36] A. Spadoni, M. Ruzzene, Elasto-static micropolar behavior of a chiral auxetic lattice, J. Mechanics and Physics of Solids **60**, 156-171 (2012).

[37] X. N. Liu, G. L. Huang, G. K. Hu, Chiral effect in plane isotropic micropolar elasticity and its application to chiral lattices, J. Mechanics and Physics of Solids **60**, 1907-1921 (2012).

[38] C. S. Ha, M. E. Plesha, R. S. Lakes, Chiral three dimensional lattices with tunable Poisson's ratio, Smart Materials and Structures, **253**, 054005 (6pp) (2016).

[39] C. S. Ha, M. E. Plesha, R. S. Lakes, Chiral three-dimensional isotropic lattices with negative Poisson's ratio, Physica Status Solidi B, **253**, (7), 1243-1251 (2016).

[40] M. Warner, E. M. Terentjev, R. B. Meyer, and Y. Mao, Untwisting of a Cholesteric Elastomer by a Mechanical Field, Phys. Rev. Lett. **102**, 217601 (2009).

[41] D. Royer, and E. Dieulesaint, Elastic and piezoelectric constants of trigonal selenium and tellurium crystals, Journal of Applied Physics **50**, 4042-4044 (1979).

[42] R. S. Lakes, Third-rank piezoelectricity in isotropic chiral solids, Appl. Phys. Lett., **106**, 212905, May (2015).